

On the nature of photospheric horizontal magnetic field increase in major solar flares

LIJUAN LIU,^{1,2,3} ZHENJUN ZHOU,^{1,2} YUMING WANG,^{4,2} XUDONG SUN,⁵ AND GUOQIANG WANG⁶

¹*Planetary Environmental and Astrobiological Research Laboratory (PEARL), School of Atmospheric Sciences, Sun Yat-sen University, Zhuhai, Guangdong, 519082, China*

²*CAS center for Excellence in Comparative Planetology, China*

³*Key Laboratory of Tropical Atmosphere-Ocean System, Sun Yat-sen University, Ministry of Education, Zhuhai, China*

⁴*CAS Key Laboratory of Geospace Environment, Department of Geophysics and Planetary Sciences, University of Science and Technology of China, Hefei, Anhui, 230026, China*

⁵*Institute for Astronomy, University of Hawai'i at Manoa, Pukalani, HI 96768, USA*

⁶*Institute of Space Science and Applied Technology, Harbin Institute of Technology, Shenzhen, China*

ABSTRACT

Rapid increase of horizontal magnetic field (B_h) around the flaring polarity inversion line is the most prominent photospheric field change during flares. It is considered to be caused by the contraction of flare loops, the details behind which is still not fully understood. Here we investigate the B_h -increase in 35 major flares using HMI high-cadence vector magnetograms. We find that B_h -increase is always accompanied by the increase of field inclination. It usually initiates near the flare ribbons, showing step-like change in between the ribbons. In particular, its evolution in early flare phase shows close spatio-temporal correlation to flare ribbons. We further find that B_h -increase tends to have similar intensity in confined and eruptive flares, but larger spatial-extent in eruptive flares in a statistical sense. Its intensity and timescale have inverse and positive correlations to the initial ribbon separations, respectively. The results altogether are well consistent with a recent proposed scenario which suggests that the reconnection-driven contraction of flare loops enhances photospheric B_h according to the ideal induction equation, providing statistical evidence to the reconnection-driven origin for B_h -increase for the first time.

1. INTRODUCTION

Solar flares are known as the process of sudden energy release caused by magnetic reconnection (Priest & Forbes 2002). They occur on time scale as short as minutes, during which the coronal magnetic field reorganizes rapidly, involving the eruption of magnetic flux rope above and the formation of post-flare loops below the reconnecting current sheet as suggested by the standard flare model (CHSKP model, see review in Shibata & Magara 2011). The process, which occurs rapidly in tenuous corona, is not expected to exert considerable influence on photosphere since the latter is much denser (Aulanier 2016). However, observations have revealed a counter-intuitive fact that the photospheric magnetic field does undergo appreciable changes during flares (see review in Wang & Liu 2015, Toriumi & Wang 2019). The most prominent change is the abrupt, permanent increase of horizontal magnetic field (B_h) around the flaring polarity inversion line (PIL), often accompanied by B_h decrease in the peripheral sunspots (e.g., Wang et al. 2002, Sudol & Harvey

2005, Wang et al. 2012, Sun et al. 2017). Different from B_h , the vertical magnetic field (B_z) varies much less without clear pattern (Sun et al. 2017). Accompanied by the field changes, other photospheric signatures, such as darkening of near-PIL penumbrae and weakening of peripheral penumbrae (Liu et al. 2005, Wang et al. 2013), sunspot rotation (Wang et al. 2014), increase of field shear and inclination (Wang et al. 2012), etc., are also found.

The observations indicate an instant feedback from coronal eruptions to the photosphere, the nature of which is still not fully understood. B_h -increase around the flaring PIL, accompanied by the increase of field inclination, can be naturally interpreted by the “tilt” or contraction of flare loops above the core region. This is supported by the topological analysis of coronal magnetic field during flares, which reveals the field across PIL collapses toward photosphere after flares (Li et al. 2011, Sun et al. 2012, Liu et al. 2012). But what exactly causes the field collapse? “Magnetic implosion” conjecture is often cited as an explanation (Hudson 2000). It suggests that the coronal loops must contract to compensate for energy decrease in eruption region according to the rule of energy conservation. The sudden change in corona may also excite an MHD wave which propagates downward and partially penetrates the photosphere to

distort the field there (Hudson et al. 2008, Fletcher & Hudson 2008, Wheatland et al. 2018). Moreover, the photospheric field change is suggested useful for estimating the total Lorentz force change during eruptions, therefore useful for estimating the force impulse associated with the coronal mass ejection (CME) momentum (Fisher et al. 2012, Hudson et al. 2012).

The details about how flare loops contraction affects the photospheric field are not entirely clear. The implosion model mainly predicts the contraction of coronal loops, which seems not guarantee the field near photosphere to respond in a similar way (Sun et al. 2017). Moreover, although implosion is often related to observed in-eruption contraction of non-erupting coronal loops (e.g., Gosain 2012, Simões et al. 2013, Wang et al. 2018), its relation to observed flare loops contraction (Ji et al. 2007, Liu et al. 2013) needs clarification. Besides, if the flare loops contraction is just morphological, it may only affect B_h at the loops footpoints, forming disconnected, ribbon-like regions of B_h -increase alongside the PIL, while the observed B_h -increase occurs in a whole region covering the PIL. Further detailed explanation is needed. Recently, Barczynski et al. (2019) analyzed the 3D magnetic field in a generic MHD simulation of an eruptive flare to draw more details of above process. They concluded that the photospheric B_h -increase is resulted from the reconnection-driven contraction of flare loops, which can be well explained by the ideal induction equation ($\frac{\partial B_{x,y}}{\partial t} = -B_{x,y} \frac{\partial u_z}{\partial z}$; u_z is the vertical plasma velocity): the newly-reconnected flare loops which possess strong line curvature and thus strong magnetic tension at their apex, may contract downward and drive reconnection jet. The contraction process will brake when approaching the photosphere, resulting in negative $\frac{\partial u_z}{\partial z}$ which enhances B_h under the loops through induction equation. The work stressed the role of flare-reconnection in enhancing B_h . Similar conclusions are drawn by a few observations, e.g., Liu et al. (2018) found a co-temporal and co-spatial evolution trend between B_h -increase region and flare ribbons; Wang & Liu (2021) discovered that the photospheric field inclination and running penumbral waves were affected by coronal reconnection. In addition to these case studies, extensive statistical research is needed.

To explore more details of photospheric field changes in flares, especially the role that flare-reconnection plays, we perform a statistical research on the most prominent change - B_h -increase - in 35 major flares using the high-cadence magnetograms provided by Helioseismic and Magnetic Imager (HMI; Hoeksema et al. 2014, Sun et al. 2017) onboard *Solar Dynamics Observatory* (SDO). We mainly compared the characteristics of B_h -increase and flare ribbons.

2. DATA

HMI measures the Stokes parameters at six wavelengths along Fe I 6173 Å absorption line, based on which the photospheric vector magnetic field is derived by the Very Fast Inversion of the Stokes Vector algorithm (Hoeksema et al. 2014). The data has a plate scale of 0''5, with a cadence of 720-s for the regular product, and of 90-s or 135-s for the high-cadence product. We select 35 major flares (all larger than M6.0-class, see Table 1), including 9 confined and 26 eruptive cases, from the first release of high-cadence data (Sun et al. 2017). For each flare, we create a set of cutout-maps from full-disk magnetograms to track its source active region (AR). The cutout-maps are re-projected from the native Helioprojective-Cartesian coordinate to a local Cartesian cylindrical-equal-area coordinate for easier handling (Sun 2013). The formal uncertainty in the spectral line inversion is propagated as error to the data.

We check the flares' CME association through inspecting the *SOHO* LASCO CME catalog¹, and analyze the flare ribbons properties using the 1600 Å images provided by Atmospheric Imaging Assembly (AIA; Lemen et al. 2012) onboard *SDO*. The data has a plate scale of 0''6 and a cadence of 24-s. The saturation that sometimes appears in AIA images in major flares is corrected by replacing each problematic pixel with a value linearly interpolated from the pixel's two unsaturated values before and after the saturation period (Kazachenko et al. 2017).

3. RESULTS

3.1. An example of B_h -increase

3.1.1. Methods

We analyze the evolution of flare-related B_h -increase case-by-case. An M6.6-class flare (SOL2015-06-22T17:39, case 33 in Table 1) is shown as an example (Figure 1 and Figure 2). We firstly scrutinize the vector magnetograms and construct two masks of B_h -increase, including a post-flare mask used to pinpoint the final B_h -increase region (Figure 1(a)), and a spatio-temporal mask used to check the propagation of B_h -increase (Figure 1(b)). The first mask consists of pixels where post-flare B_h -increase exceeds 120 Gauss (red patches enclosed by darkgreen contours in Figure 1(a)). The pixels are identified from a B_h difference image constructed by subtracting a pre-flare B_h map from a post-flare B_h map. The threshold for identifying B_h -increase, 120 Gauss, is slightly higher than HMI B_h uncertainty (Hoeksema et al. 2014). The second mask records the time when B_h -increase firstly reaches 120 Gauss in each pixel. A similar method is performed on AIA 1600 Å images to obtain the spatio-temporal mask for flare ribbons (Figure 1(c)). We use a threshold

¹ https://cdaw.gsfc.nasa.gov/CME_list/index.html

several times larger than the median pixel value of all 1600 Å maps to identify the ribbon pixels (Kazachenko et al. 2017).

We further track the fronts of B_h -increase region and flare ribbons to compare their propagation details. In each polarity, we select a representative point from the region front (either of B_h -increase region or of flare ribbons), and track the point through measuring its distance to the PIL. The representative point (cyan squares in Figure 1(a)) is determined as the intersection between region boundary and a slice perpendicular to the source PIL (S_p and S_n in Figure 1(a)). We choose the slices as close as possible to ribbons initiation positions. The results are shown in Figure 2(a).

We also calculate a few parameters from the B_h -increase region to quantify its evolution, including the area, mean B_h (\bar{B}_h), total B_h (ΣB_h), mean shear angle (\bar{S}), mean inclination angle ($\bar{\theta}$; with respect to solar normal), and the proxy of total photospheric excess magnetic energy density (ρ_{tot} , Wang et al. 1996, Leka et al. 2003). Calculation details are shown in Table 2. \bar{B}_h quantifies the intensity, while ΣB_h and area measure the extension, of B_h -increase. $\bar{\theta}$ measures the field inclination. \bar{S} and ρ_{tot} quantify the deviation of magnetic field from its potential state to some extent. If applicable, the temporal evolution of a parameter P is further fitted by a step-like function

$$P(t)=a+bt+c\left\{1+\frac{2}{\pi}\arctan[n(t-t_m)]\right\}, \quad (1)$$

where a , b , c , n , and t_m are free parameters (Sudol & Harvey 2005, Sun et al. 2017). The term $a+bt$ indicates the linear evolution in addition to step-like change; the parameter change is calculated by $\Delta P=2c$; the change timescale is given by $\tau=\pi/n$; t_m is the change mid-time. We use IDL procedure *mpfit.pro*² to perform the fitting. The parameters evolution, with errors propagated from the formal uncertainty, are shown in Figure 2(b)-(g). The *GOES* 1-8 Å flux is shown for comparison (blue curve in Figure 2(g)).

3.1.2. Features of B_h -increase

The high-cadence data reveals the evolution details of B_h -increase. It is seen that B_h -increase starts from two kernels alongside the PIL (darkblue patches in Figure 1(b) and yellow contours in Figure 1(c)), roughly coinciding with the flare ribbons initial positions. It then extends out (see Figure 1-associated movie), filling a whole region covering part PIL. Evolution of the regions fronts (Figure 2(a)) further reveals that B_h -increase does follow the ribbons propagation in early flare phase, but remains almost still afterwards while the ribbons propagate further.

For the parameters quantifying B_h -increase (Figure 2(b)-(g)), the area reaches around 443.6 Mm² after flare. \bar{B}_h and ΣB_h both show step-like increase which can be fitted by Equation 1. The fitting reveals that \bar{B}_h begins to increase 11.6 minutes after the flare start (*GOES* start time), and lasts for 24.9 minutes. Its post-flare change ($\Delta\bar{B}_h$) is 235.1 Gauss. The fitting of ΣB_h yields similar results. Its post-flare change ($\Delta\Sigma B_h$) is 10.4×10^{20} Mx. $\bar{\theta}$, \bar{S} , and ρ_{tot} also show step-like change here, but their evolution in most other cases are too complicated to fit. To avoid the bias, we calculate the three parameters' change here, as well as in other cases, by subtracting the pre-flare value from the post-flare value instead of fitting (see details in Table 2). Here their changes ($\Delta\bar{\theta}$, $\Delta\bar{S}$, and $\Delta\rho_{tot}$) are 4.5°, 2.1°, and 4.5×10^{22} erg cm⁻¹, respectively, indicating the field in B_h -increase region becomes more inclined and sheared after the flare.

3.2. Statistics of B_h -increase

Using the above methods, we identify B_h -increase in all cases and perform a statistical research. We found the post-flare change of \bar{B}_h , $\Delta\bar{B}_h$, ranges from 144.5 G to 573.4 G in the sample, having a median of 263.5 G (Figure 3(a)). The change of ΣB_h , $\Delta\Sigma B_h$, has a median of 5.4×10^{20} Mx (Figure 3(b)). The area has a median of 176.3 Mm² (Figure 3(c)). The change of $\bar{\theta}$ ($\Delta\bar{\theta}$) shows increase in all cases as well, having a median of 5.2° (Figure 3(d)). The change of \bar{S} ($\Delta\bar{S}$) shows increase in about 2/3 (23) cases. Its median is 1.3° (Figure 3(e)). The change of ρ_{tot} ($\Delta\rho_{tot}$) displays increase in 94% (33) cases, having a median of 1.9×10^{22} erg cm⁻¹ (Figure 3(f)). The timescale of B_h -increase, τ , ranges from 5.8 minutes to 84.4 minutes, having a median of 24.4 minutes (Figure 3(g)). The start time of B_h -increase, t_{start} , is generally small, having a median of 3.0 minutes (Figure 3(h)). τ and t_{start} are quoted from the \bar{B}_h evolution fitting. The results are consistent with previous observations that the field in B_h -increase region becomes more inclined and sheared after flares.

When dividing the cases into confined and eruptive groups (Figure 3), the intensive parameter of B_h -increase, $\Delta\bar{B}_h$, shows very close medians in the two sub-samples, suggesting a weak statistical difference. By contrast, the extensive parameters, $\Delta\Sigma B_h$ and area, shows larger medians in eruptive flares. Similarly, $\Delta\bar{S}$ and $\Delta\rho_{tot}$, also have larger medians in eruptive flares. $\Delta\bar{\theta}$ and t_{start} show no significant statistical difference in two sub-samples. Only τ has larger median in confined flares. These suggest that B_h -increase occurs in either confined or eruptive flares, having similar intensity in both kinds but larger spatial-extent in eruptive flares.

We also compare the propagation of B_h -increase region and flare ribbons in all cases through tracking their fronts (Figure 4). It is seen that B_h -increase always appears after the flare ribbons appear, with 60% (21)

² <https://pages.physics.wisc.edu/~craigm/idl/fitting.html>

cases initiating quite close to the ribbons (with separation ≤ 5 Mm). The region then widens, manifested as front progressing, in early phase of most flares. Only in 7 cases (e.g., case 4), the region front barely moves after appearance (progressing ≤ 2 Mm). Throughout the flare, the B_h -increase region evolves in between the straight parts of flare ribbons, and stops growing before the ribbons stop progressing, as suggested by the increasing distance between their fronts. The results indicate that in general, B_h -increase and flare ribbons have close spatio-temporal correlations in early flare phase.

The summed value of distances from ribbons fronts to the PIL in both positive and negative polarities (green curves in Figure 4) represents the separation between flare ribbons. Since the straight parts of flare ribbons highlight the footpoints of flare loops as suggested in the 3D extension of standard flare model (Aulanier et al. 2012, Janvier et al. 2013), the ribbons separation can indicate the loops height if consider a nearly-semicircular shape of the loops (Fletcher & Hudson 2008, Thalmann et al. 2015, Kusano et al. 2020). Therefore the ribbons separation obtained in very early flare stage, defined as initial ribbons separation (IRS) here (see calculation details in Table 2), indicates the height where early flare loops are formed, i.e., where flare reconnection initiates. We then check the correlation between the IRS and B_h -increase parameters. Interestingly, we find a rough inverse correlation between $\Delta\bar{B}_h$ and IRS (Figure 5(a)). Their relation can be roughly fitted by an exponential decaying function in the form of $\Delta\bar{B}_h = 220.0 + 357.6e^{-0.36 \times IRS}$ (reduced chi-square $\chi_r^2 = 0.61$). Given the large uncertainty of $\Delta\bar{B}_h$, it is more appropriate to see the fitting only as a reference. Moreover, the timescale τ of B_h -increase shows a significant correlation with IRS (cc=0.71; Figure 5(b)). These indicate that smaller initial ribbon separation tends to be accompanied by B_h -increase of larger intensity and shorter timescale.

We also check the correlation between flare magnitude and the parameters, and find an overall weak trend that larger flares are accompanied by B_h -increase of larger intensity and shorter timescale (Figure 5(c)-(d)).

4. SUMMARY AND DISCUSSION

In this work, we investigate the photospheric horizontal field increase in 35 major flares using the HMI high-cadence field data, and obtain the following results which may deepen our understanding to flare-related B_h -increase:

- 1) B_h -increase appears in every case, accompanied by the field inclination increase. This supports that the magnetic field rooted in this region becomes more inclined after the flare.
- 2) B_h -increase usually initiates near the flare ribbons, showing step-like change which evolves in

a limited region in between the straight parts of flare ribbons. In particular, its evolution in early flare phase shows close spatio-temporal correlation to flare ribbons. Since the ribbons highlight loops footpoints, these suggest that B_h -increase is closely related to flare loops evolution.

- 3) The intensive parameter of B_h -increase (mean B_h) shows no statistical difference in confined and eruptive flares, while the extensive parameters (total B_h and area) tend to be larger in eruptive flares. These suggest that the process leading to B_h -increase tends to affect larger photospheric area during CME-associated flares.
- 4) The intensity and timescale of B_h -increase are inversely and positively correlated to the initial ribbons separation, respectively. Since initial ribbon separation indicates the height where flare-reconnection initiates (see Section 3.2), these suggest that the process leading to B_h -increase may start along with the flare-reconnection, and then propagates downward, resulting in faster and stronger photospheric effect when the propagating path is shorter (lower reconnection height).

The above results altogether support that B_h -increase is resulted from the flare reconnection-driven contraction of flare loops, governed by induction equation (Barczynski et al. 2019). The first finding (item 1) supports the occurrence of flare loops contraction, consistent with previous studies (see Section 1). The second further supports a flare loops-related origin for B_h -increase. The third has a natural interpretation from the standard flare model: the upward motion of CMEs in eruptive flares tends to result in more flare loops which may sweep wider photospheric area. The fourth is well explained when considering the induction equation: smaller initial ribbon separation indicates lower, shorter flare loops formed in early flare phase, which may relax downward faster and brake sharply with the tension-driven jet, resulting in larger $\frac{\partial u_z}{\partial z}$ which amplifies photospheric B_h more quickly and significantly. The higher, longer loops formed later tend to behave oppositely, explaining why B_h -increase only follows the ribbons in early flare phase. This is analogous to the phenomenon revealed in simulation: B_h -increase occurs slower in regions later swept by current ribbons (Barczynski et al. 2019). Note the latter three findings are systematically identified here for the first time. Besides above results, the identified shear increase is also consistent with the shear transfer process suggested in 3D flare model.

Our results suggest that B_h -increase is consistent with the standard flare model. Although the model is proposed for eruptive flares, the difference of B_h -increase in confined and eruptive flares identified here is not strik-

ing (see item 3 above). This might be because even some confined flares may still involve confined flux rope eruptions. A flare showing observable signatures of confined eruption of possible flux ropes (e.g., filaments or hot channels) is called failed eruption (Ji et al. 2003). In that case, the flux rope also rises, leading to the formation of current sheet below, but fails to propagate out due to strong confinement above (Török & Kliem 2005). The flare thus tends to have similar properties to an eruptive flare (Harra et al. 2016). However, its ribbons may sweep less large photospheric area as the flux rope stops ascending earlier, consistent with our findings above (item 3). For the confined flare not involving a flux rope, observations suggest that the flare-reconnection may occur between multiple magnetic systems, and about one third of observed confined flares belongs to this category (Li et al. 2019). Considering that we have around 27% (9/35) confined flares, the portion of the category is quite small, which may not significantly affect our statistical results despite what their B_h -increase properties are.

The implosion conjecture (Hudson 2000) is often referred to explain B_h -increase (see Section 1). Although our results support a reconnection-driven origin for B_h -increase, the implosion should still be consistent with the process since it is just a restatement of the universal rule of energy conservation. The conservation of momentum during coronal eruptions (Hudson et al. 2012, Fisher et al. 2012) is also referred to explain the flare-related B_h -increase sometimes (e.g., Barczynski et al. 2019, Wang & Liu 2021). But to our understanding, the CME momentum, and corresponding downward momentum, is related to the photospheric field change through Lorentz force change under some approximation, and only sets a lower limit to Lorentz force impulse (Fisher et al. 2012). It may not be appropriate to take the momentum conservation as an independent cause for B_h -increase. The identified relatively larger total B_h -increase in eruptive flares indeed suggests a larger Lorentz force change in CMEs.

To summarize, our results support that B_h -increase during flares is very likely to be caused by the reconnection-driven contraction of flare loops, and is governed by induction equation.

Table 1. Flare information and B_h -increase characteristics.

No.	Flare				Parameters									
	Class	Start	Location	AR	CME ^a	$\Delta \bar{B}_h$ Gauss	$\Delta \Sigma B_h$ $\times 10^{20}$ Mx	Area Mm ²	$\Delta \bar{\theta}$ degree	$\Delta \bar{S}$ degree	$\Delta \rho_{total}$ $\times 10^{22}$ erg cm ⁻¹	τ mins	t_{start} mins	IRS ^b Mm
1	M6.6	SOL2011-02-13T17:28	S20E05	11158	Y	334.5±98.2	3.4±1.0	101.6±3.9	3.0±2.0	1.0±2.1	2.04±0.02	0.6	16.2	3.4±0.2
2	X2.2	SOL2011-02-15T01:44	S20W12	11158	Y	294.2±97.3	7.8±2.6	252.5±11.4	6.0±2.3	3.5±2.5	4.66±0.04	1.4	12.4	4.1±0.0
3	X1.5	SOL2011-03-09T23:13	N08W11	11166	N	261.8±73.2	1.3±0.4	52.3±2.7	2.0±2.3	-4.7±2.4	0.25±0.02	2.8	6.4	5.8±0.3
4	M9.3	SOL2011-07-30T02:04	N14E35	11261	N	444.0±75.6	2.7±0.5	59.8±4.4	6.3±3.7	-8.2±4.2	1.18±0.03	3.2	5.8	4.3±0.2
5	M6.0	SOL2011-08-03T13:17	N16W30	11261	Y	331.1±179.9	6.9±3.8	206.2±11.8	5.7±3.3	2.2±4.1	1.88±0.02	1.1	45.1	14.0±0.8
6	M9.3	SOL2011-08-04T03:41	N16W38	11261	Y	263.7±85.1	6.7±2.4	258.5±14.7	4.0±3.8	1.3±4.5	3.64±0.03	5.7	11.9	6.0±0.3
7	X2.1	SOL2011-09-06T22:12	N14W18	11283	Y	382.0±84.6	6.6±1.6	173.9±8.7	6.3±3.3	2.1±4.1	3.41±0.03	3.8	10.7	6.5±0.8
8	X1.8	SOL2011-09-07T22:32	N14W31	11283	Y	324.1±98.9	6.4±2.2	185.0±14.4	4.9±4.8	-2.1±5.7	1.75±0.03	3.4	10.6	2.3±1.2
9	M8.7	SOL2012-01-23T03:38	N33W21	11402	Y	215.1±154.5	3.6±2.7	166.3±17.4	7.1±8.8	-7.8±9.7	1.06±0.03	5.3	42.9	16.1±2.1
10	X5.4	SOL2012-03-07T00:02	N18E31	11429	Y	278.4±168.1	120.5±13.2	720.6±51.8	9.9±3.5	2.4±3.7	11.02±0.08	5.7	18.0	3.4±1.0
11	X1.3	SOL2012-03-07T01:05	N15E26	11429	Y	186.3±142.0	3.4±2.8	176.3±18.2	5.3±6.0	2.7±6.6	1.28±0.05	0.3	11.8	24.6±0.9
12	M6.3	SOL2012-03-09T03:22	N15W03	11429	Y	224.2±210.5	6.2±5.9	275.5±18.6	3.2±4.3	-2.5±5.1	2.13±0.03	2.2	42.8	2.5±0.2
13	M8.4	SOL2012-03-10T17:15	N17W24	11429	Y	241.6±80.1	9.2±3.1	405.7±25.7	7.2±5.2	3.6±6.0	5.09±0.03	0.8	29.2	3.7±1.4
14	X1.4	SOL2012-07-12T15:37	S13W03	11520	Y	247.9±172.8	7.2±4.9	292.2±18.5	2.3±5.1	-1.0±8.8	1.62±0.02	17.2	84.4	61.8±0.0
15	M6.5	SOL2013-04-11T06:55	N09E13	11719	Y	167.8±228.7	0.6±0.8	36.8±3.6	3.8±4.6	2.6±7.1	0.12±0.01	0.2	40.1	10.3±1.2
16	M9.3	SOL2013-10-24T00:21	S09E10	11877	N	241.1±83.3	2.9±1.0	118.2±6.9	3.2±3.0	2.9±4.5	1.40±0.02	0.1	12.3	28.9±1.1
17	X3.3	SOL2013-11-05T22:07	S12E44	11890	Y	569.4±114.7	4.8±1.1	81.5±3.7	5.2±2.7	3.4±2.6	4.83±0.05	3.5	8.1	2.8±1.6
18	X1.1	SOL2013-11-08T04:20	S13E15	11890	Y	409.7±92.9	4.4±1.0	107.7±4.5	4.8±2.0	3.7±2.1	3.42±0.03	0.6	11.5	3.8±1.2
19	X1.1	SOL2013-11-10T05:08	S13W13	11890	Y	367.4±80.5	3.7±0.9	106.0±5.1	5.9±3.0	1.0±3.7	3.00±0.03	0.7	10.2	1.5±0.8
20	M9.9	SOL2014-01-01T18:40	S16W45	11936	Y	257.9±209.1	3.6±3.4	155.2±20.8	21.4±12.2	-4.4±13.1	-0.29±0.02	1.4	26.7	6.2±0.5
21	X1.2	SOL2014-01-07T18:04	S12W08	11944	Y	185.4±118.1	0.8±0.5	42.5±2.7	1.8±2.2	1.3±4.9	0.01±0.00	9.1	46.8	44.6±3.2
22	X1.0	SOL2014-03-29T17:35	N10W32	12017	Y	257.4±130.8	3.3±2.1	138.7±12.4	7.0±5.6	-3.0±6.7	0.19±0.02	3.2	18.0	2.5±0.4
23	X1.6	SOL2014-09-10T17:21	N11E05	12158	Y	208.5±173.2	8.0±7.0	381.7±22.4	3.4±2.6	0.1±4.1	1.88±0.02	1.2	49.3	24.0±1.1
24	M8.7	SOL2014-10-22T01:16	S13E21	12192	N	263.5±169.8	6.9±4.6	261.9±13.1	3.2±2.3	-2.6±2.6	0.71±0.02	5.4	53.0	51.3±1.9
25	X1.6	SOL2014-10-22T14:02	S14E13	12192	N	268.5±262.0	0.5±0.6	17.4±0.8	0.9±2.5	0.5±2.7	0.25±0.01	4.2	45.3	32.2±2.2
26	X3.1	SOL2014-10-24T21:07	S22W21	12192	N	144.5±87.3	3.6±2.2	250.1±21.4	5.4±4.5	-0.0±5.9	0.20±0.02	0.1	35.5	15.9±1.4
27	X2.0	SOL2014-10-26T10:04	S14W37	12192	N	175.5±131.0	1.4±0.8	58.2±10.5	25.4±9.8	-11.9±10.0	-0.26±0.01	24.4	33.7	28.5±0.3
28	X1.6	SOL2014-11-07T16:53	N17E40	12205	Y	375.8±263.3	11.7±8.4	309.3±19.7	6.9±3.2	0.4±3.4	4.75±0.07	3.6	35.0	6.0±2.7
29	M6.1	SOL2014-12-04T18:05	S20W31	12222	N	237.6±183.3	2.1±1.7	85.4±9.8	10.7±9.8	-6.9±11.1	0.05±0.01	1.1	36.9	11.7±0.4
30	M6.9	SOL2014-12-18T21:41	S11E10	12241	Y	243.2±162.3	9.1±6.1	374.0±16.5	4.2±2.8	1.3±3.6	2.80±0.03	0.1	38.6	6.0±0.2
31	X1.8	SOL2014-12-20T00:11	S19W29	12242	Y	267.4±134.4	14.8±7.6	547.7±36.4	4.8±3.7	1.8±4.5	7.40±0.06	3.1	24.4	3.1±0.0
32	X2.2	SOL2015-03-11T16:11	S17E22	12297	Y	326.2±144.8	6.6±2.8	207.0±9.8	3.2±2.2	3.2±2.2	5.49±0.04	3.0	17.7	13.9±1.4
33	M6.6	SOL2015-06-22T17:39	N13W06	12371	Y	235.1±55.8	10.4±2.5	443.6±15.6	4.5±1.8	2.1±2.2	7.67±0.04	11.6	24.9	4.6±0.0

Table 1 continued

Table 1 (continued)

No.	Flare	Parameters
34	X2.2 SOL2017-09-06T08:57 S08W32 12673 N	481.4±236.9 5.4±3.0 105.2±11.0 8.3±3.6 5.8±4.9 6.72±0.47 5.1 12.1 5.9±0.3
35	X9.3 SOL2017-09-06T11:53 S09W34 12673 Y	573.4±184.3 16.6±6.7 276.8±31.2 8.5±4.8 2.5±5.2 16.83±0.94 2.6 7.3 2.5±1.0

^aCME association of the flares. "Y" ("N") refers to yes (no).

^bIRS (initial ribbons separation) is averaged in the very early flare stage, with σ taken as the error. See calculation details for all parameters in Table 2.

ACKNOWLEDGMENTS

We thank Haisheng Ji for the helpful discussions. We thank our anonymous referee for his/her constructive comments that significantly improved the manuscript. We acknowledge the *SDO*, *SOHO*, and *GOES* missions for providing quality observations. L.L. is supported by the Guangdong Basic and Applied Basic Research Foundation.

REFERENCES

- Alissandrakis, C. E. 1981, *A&A*, 100, 197. <http://adsabs.harvard.edu/full/1981A%7B%7D26A...100..197A>
- Aulanier, G. 2016, *Nature Physics*, 12, 998, doi: [10.1038/nphys3938](https://doi.org/10.1038/nphys3938)
- Aulanier, G., Janvier, M., & Schmieder, B. 2012, *A&A*, 543, A110, doi: [10.1051/0004-6361/201219311](https://doi.org/10.1051/0004-6361/201219311)
- Barczynski, K., Aulanier, G., Masson, S., & Wheatland, M. S. 2019, *ApJ*, 877, 67, doi: [10.3847/1538-4357/ab1b3d](https://doi.org/10.3847/1538-4357/ab1b3d)
- Bobra, M. G., Sun, X., Hoeksema, J. T., et al. 2014, *SoPh*, 289, 3549, doi: [10.1007/s11207-014-0529-3](https://doi.org/10.1007/s11207-014-0529-3)
- Fisher, G. H., Bercik, D. J., Welsch, B. T., & Hudson, H. S. 2012, *SoPh*, 277, 59, doi: [10.1007/s11207-011-9907-2](https://doi.org/10.1007/s11207-011-9907-2)
- Fletcher, L., & Hudson, H. S. 2008, *ApJ*, 675, 1645, doi: [10.1086/527044](https://doi.org/10.1086/527044)
- Gosain, S. 2012, *ApJ*, 749, doi: [10.1088/0004-637X/749/1/85](https://doi.org/10.1088/0004-637X/749/1/85)
- Harra, L. K., Schrijver, C. J., Janvier, M., et al. 2016, *SoPh*, 291, 1761, doi: [10.1007/s11207-016-0923-0](https://doi.org/10.1007/s11207-016-0923-0)
- Hoeksema, J. T., Liu, Y., Hayashi, K., et al. 2014, *SoPh*, 289, 3483, doi: [10.1007/s11207-014-0516-8](https://doi.org/10.1007/s11207-014-0516-8)
- Hudson, H. S. 2000, *ApJ*, 531, L75, doi: [10.1086/312516](https://doi.org/10.1086/312516)
- Hudson, H. S., Fisher, G. H., & Welsch, B. T. 2008, in *Subsurface and Atmospheric Influences on Solar Activity*, Vol. 383, 221. <http://adsabs.harvard.edu/pdf/2008ASPC..383..221H>
- Hudson, H. S., Fletcher, L., Fisher, G. H., Abbett, W. P., & Russell, A. 2012, *SoPh*, 277, 77, doi: [10.1007/s11207-011-9836-0](https://doi.org/10.1007/s11207-011-9836-0)
- Janvier, M., Aulanier, G., Pariat, E., & Démoulin, P. 2013, *A&A*, 555, A77, doi: [10.1051/0004-6361/201321164](https://doi.org/10.1051/0004-6361/201321164)
- Ji, H., Huang, G., & Wang, H. 2007, *ApJ*, 660, 893, doi: [10.1086/513017](https://doi.org/10.1086/513017)
- Ji, H., Wang, H., Schmahl, E. J., Moon, Y.-J., & Jiang, Y. 2003, *ApJ*, 595, L135, doi: [10.1086/378178](https://doi.org/10.1086/378178)
- Kazachenko, M. D., Lynch, B. J., Welsch, B. T., & Sun, X. 2017, *ApJ*, 845, 49, doi: [10.3847/1538-4357/aa7ed6](https://doi.org/10.3847/1538-4357/aa7ed6)
- Kusano, K., Iju, T., Bamba, Y., & Inoue, S. 2020, *Science*, 369, 587, doi: [10.1126/science.aaz2511](https://doi.org/10.1126/science.aaz2511)
- Leka, K. D., Barnes, G., & Barnes, G. 2003, *ApJ*, 595, 1277, doi: [10.1086/377511](https://doi.org/10.1086/377511)
- Lemen, J. R., Title, A. M., Akin, D. J., et al. 2012, *SoPh*, 275, 17, doi: [10.1007/s11207-011-9776-8](https://doi.org/10.1007/s11207-011-9776-8)
- Li, T., Liu, L., Hou, Y., & Zhang, J. 2019, *ApJ*, 881, 151, doi: [10.3847/1538-4357/ab3121](https://doi.org/10.3847/1538-4357/ab3121)
- Li, Y., Jing, J., Fan, Y., & Wang, H. 2011, *ApJ*, 727, L19, doi: [10.1088/2041-8205/727/1/L19](https://doi.org/10.1088/2041-8205/727/1/L19)
- Liu, C., Deng, N., Liu, Y., et al. 2005, *ApJ*, 622, 722, doi: [10.1086/427868](https://doi.org/10.1086/427868)
- Liu, C., Deng, N., Liu, R., et al. 2012, *ApJ*, 745, L4, doi: [10.1088/2041-8205/745/1/L4](https://doi.org/10.1088/2041-8205/745/1/L4)
- Liu, C., Cao, W., Chae, J., et al. 2018, *ApJ*, 869, 21, doi: [10.3847/1538-4357/aaecd0](https://doi.org/10.3847/1538-4357/aaecd0)
- Liu, W., Chen, Q., & Petrosian, V. 2013, *ApJ*, 767, doi: [10.1088/0004-637X/767/2/168](https://doi.org/10.1088/0004-637X/767/2/168)
- Priest, E. R., & Forbes, T. G. 2002, *Astronomy and Astrophysics Review*, 10, 313, doi: [10.1007/s001590100013](https://doi.org/10.1007/s001590100013)
- Shibata, K., & Magara, T. 2011, *LRSP*, 8, doi: [10.12942/lrsp-2011-6](https://doi.org/10.12942/lrsp-2011-6)
- Simões, P. J. A., Fletcher, L., Hudson, H. S., & Russell, A. J. B. 2013, *ApJ*, 777, 152, doi: [10.1088/0004-637X/777/2/152](https://doi.org/10.1088/0004-637X/777/2/152)
- Sudol, J. J., & Harvey, J. W. 2005, *ApJ*, 635, 647, doi: [10.1086/497361](https://doi.org/10.1086/497361)
- Sun, X. 2013, On the Coordinate System of Space-Weather HMI Active Region Patches (SHARPs): A Technical Note. <https://arxiv.org/abs/1309.2392>
- Sun, X., Hoeksema, J. T., Liu, Y., Kazachenko, M., & Chen, R. 2017, *ApJ*, 839, 67, doi: [10.3847/1538-4357/aa69c1](https://doi.org/10.3847/1538-4357/aa69c1)
- Sun, X., Hoeksema, J. T., Liu, Y., et al. 2012, *ApJ*, 748, 77, doi: [10.1088/0004-637X/748/2/77](https://doi.org/10.1088/0004-637X/748/2/77)
- Thalmann, J. K., Su, Y., Temmer, M., & Veronig, a. M. 2015, *ApJ*, 801, L23, doi: [10.1088/2041-8205/801/2/L23](https://doi.org/10.1088/2041-8205/801/2/L23)
- Toriumi, S., & Wang, H. 2019, *LRSP*, 16, 3, doi: [10.1007/s41116-019-0019-7](https://doi.org/10.1007/s41116-019-0019-7)

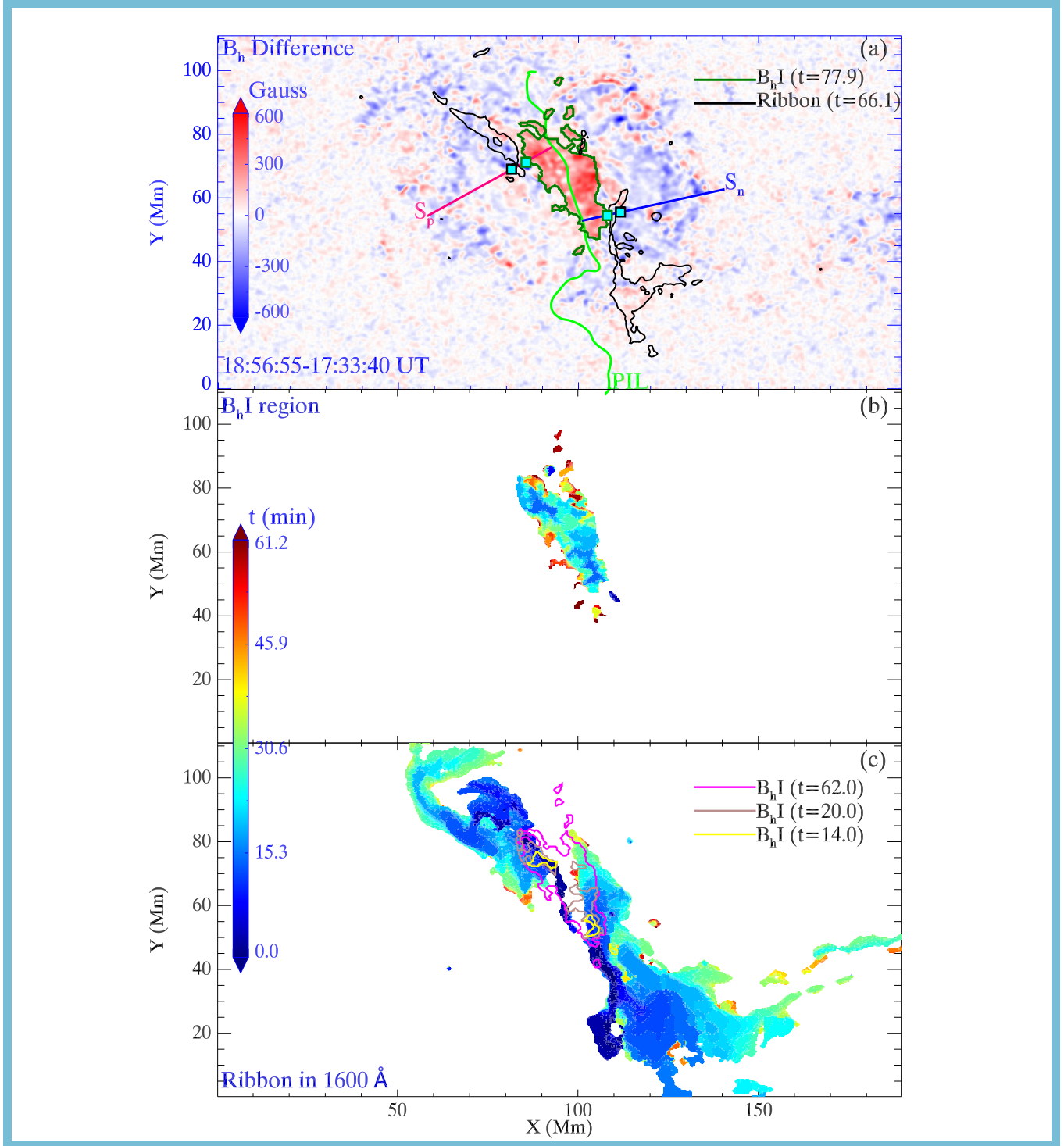


Figure 1. Evolution of B_h -increase (abbreviated as “ $B_h I$ ” in figures) in case 33. (a) A post-flare B_h difference image. The blackgreen contours outline the post-flare mask of B_h -increase (pixel value ≥ 120 Gauss); the black contours outline the flare ribbons at one moment for comparison. “ t ” (in minutes) indicates time after flare start (*GOES* start time). S_p and S_n are slices in positive and negative polarities used to determine the representative points of region fronts (cyan squares). (b)-(c) Spatio-temporal evolution masks for B_h -increase and flare ribbons, with color coded by the time elapsed from flare start. Colored contours in (c) outline B_h -increase regions at different times. The associated animation lasts from 2017-09-06T17:38 to 2017-09-06T18:56, showing the B_h -increase and ribbons evolution. Its frames have similar layout as the figure.

Table 2. Parameters quantifying B_h -increase and flare ribbons

Parameter ^a	Description	Calculation ^b	Unit	Type ^c	Change ^d
\bar{B}_h	Mean B_h	$\bar{B}_h = \frac{1}{n} \Sigma B_h$	Gauss	Intensive	$\Delta \bar{B}_h$
ΣB_h	Total B_h	$\Sigma B_h = \int B_h dA$	Mx	Extensive	$\Delta \Sigma B_h$
Area	Area	ΣdA	Mm ²	Extensive	Area
$\bar{\theta}$	Mean inclination angle	$\bar{\theta} = \frac{1}{n} \Sigma \arctan\left(\frac{B_x}{B_y}\right)$	Degree	Intensive	$\Delta \bar{\theta}$
\bar{S}	Mean shear angle	$\bar{S} = \frac{1}{n} \Sigma \arccos\left(\frac{\mathbf{B}_{pot} \bullet \mathbf{B}_{obs}}{ B_{pot} B_{obs} }\right)$	Degree	Intensive	$\Delta \bar{S}$
ρ_{tot}	Proxy for total photospheric magnetic free energy density	$\rho_{tot} = \frac{1}{8\pi} \Sigma (\mathbf{B}_{obs} - \mathbf{B}_{pot})^2 dA$	erg cm ⁻¹	Extensive	$\Delta \rho_{tot}$
τ	Timescale of B_h -increase	Quoted from the step-like function (Equation 1) fitting of \bar{B}_h evolution	Minutes		
t_{start}	Start time of B_h -increase	As above	Minutes (since flare start)		
IRS	Initial ribbon separation	Ribbons separation averaged over a duration of 5 minutes before and 1 minute after the flare start	Mm		

^a Area is calculated from B_h -increase region identified at each moment. \bar{B}_h , ΣB_h , $\bar{\theta}$, \bar{S} , and ρ_{tot} are computed using the post-flare B_h -increase mask.

^b Here n is the number of pixels of B_h -increase region. B_{obs} is the observed field; B_{pot} is the potential field calculated by a Fourier transformation method (Alissandrakis 1981). The formulae for $\bar{\theta}$, \bar{S} , and ρ_{tot} are adapted from Bobra et al. (2014).

^c “Intensive”-type and “extensive”-type parameters measure the intensity and extension of corresponding physical quantity, respectively.

^d Parameters change throughout flares. $\Delta \bar{B}_h$ and $\Delta \Sigma B_h$ are quoted from corresponding fittings. $\Delta \bar{S}$, $\Delta \bar{\theta}$, and $\Delta \rho_{tot}$ are calculated through subtracting the pre-flare value (averaged in five minutes prior to the flare) from the post-flare value (averaged in five minutes after the flare). See relevant details in Section 3.1.

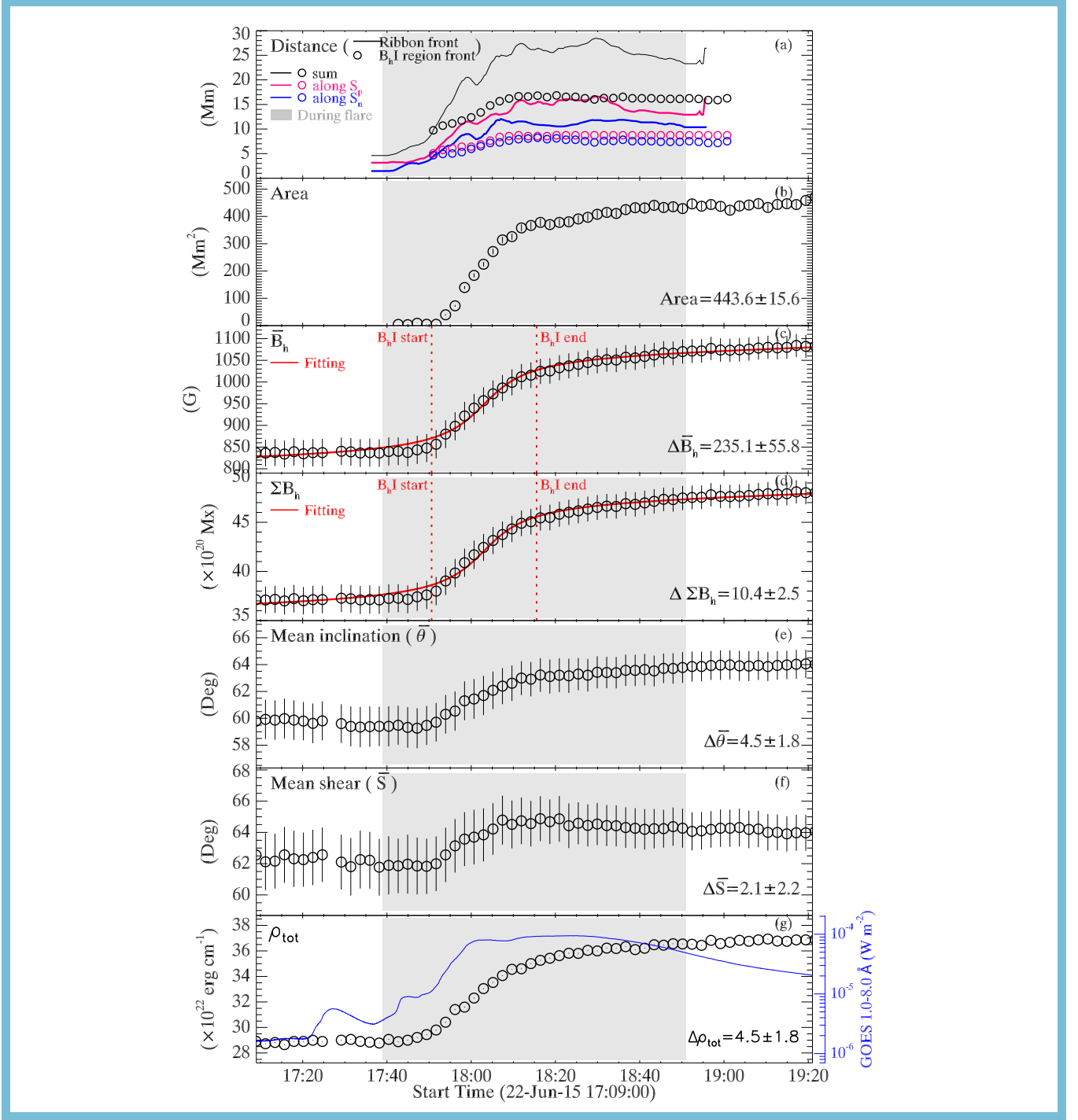


Figure 2. (a) Evolution of distances between the PIL and the fronts of B_h -increase region (circles) and flare ribbons (lines) determined by the slices in Figure 1(a). Distances in both polarities (blue and red) and as sum (black) are shown. (b)-(g) Parameters quantifying B_h -increase. The vertical-dashed lines in (c) and (d) mark the start and end timings of step-like changes obtained from fitting. The associated animation lasts from 2017-09-06T17:38 to 2017-09-06T18:56, showing parameters evolution accompanied by B_h -increase region and ribbons evolution. Each frame contains parameters panels (similar as the figure) and two insets of B_h -increase region and flare ribbons (similar as Figure 1(b)-(c)). The frame time is indicated by a vertical line in parameters panels.

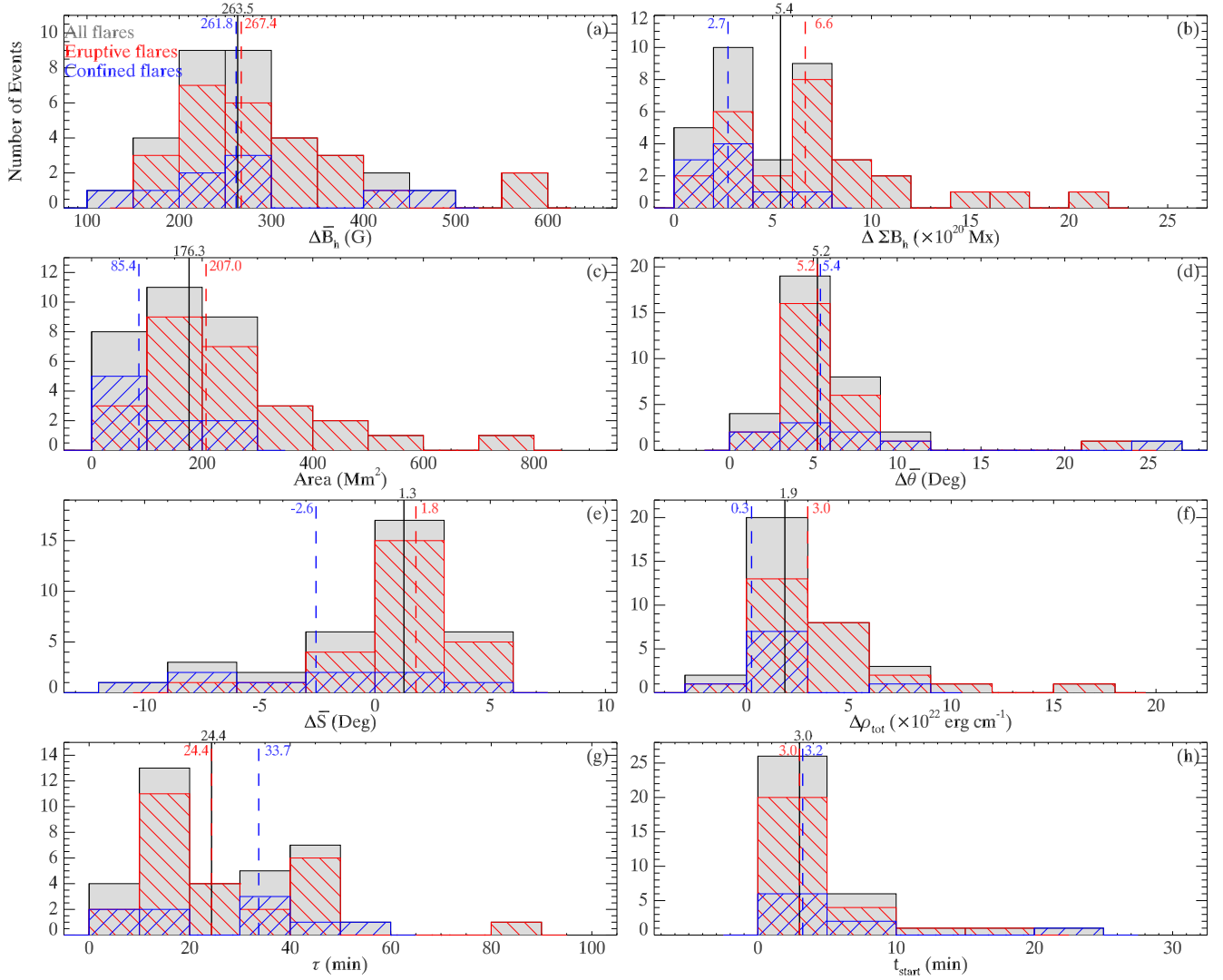


Figure 3. Distributions of the post-flare change of B_h -increase parameters. In each panel, the vertical lines, with the digits above, mark the parameters medians for corresponding samples (black, red and blue for all, eruptive and confined flares, respectively).

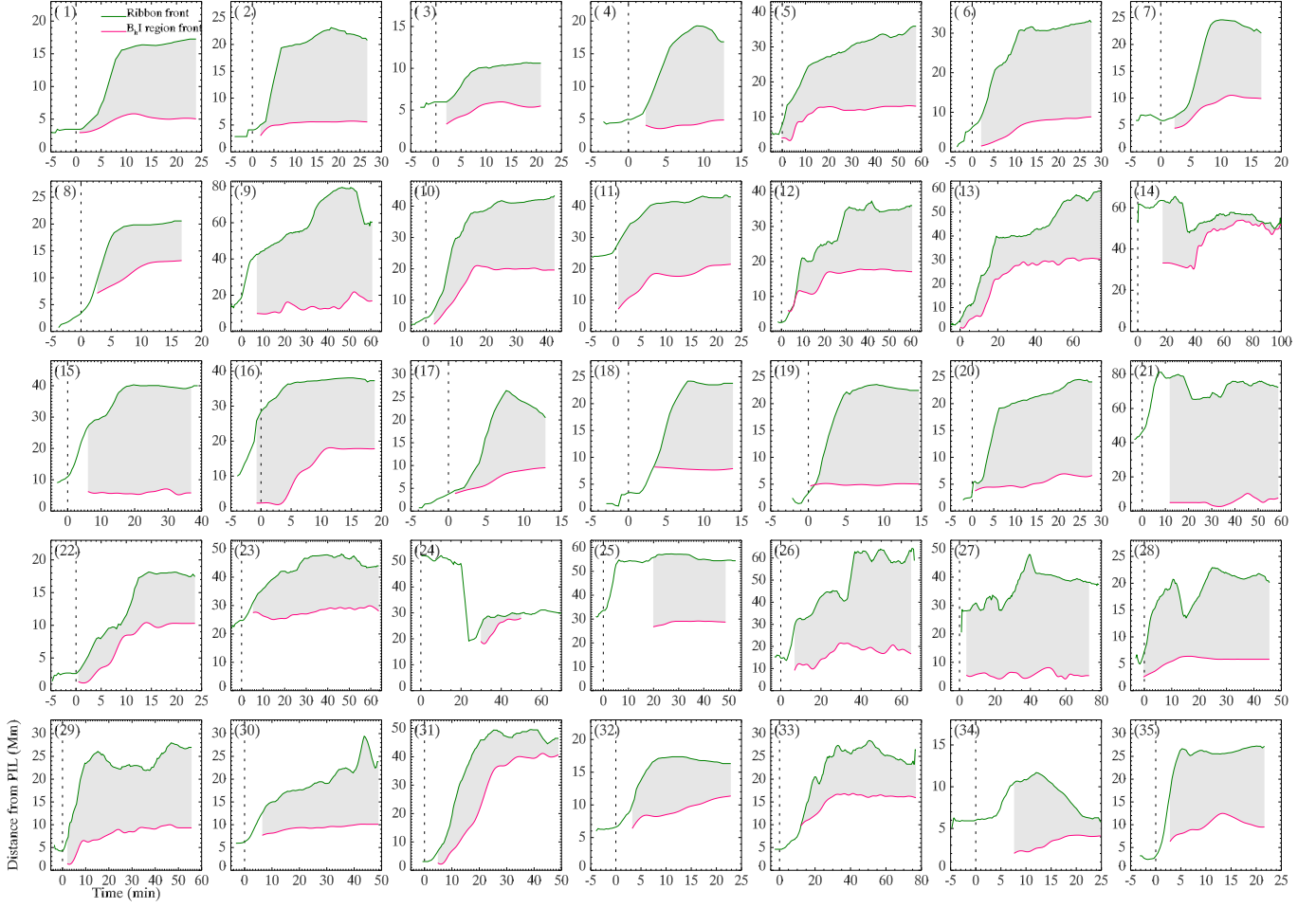


Figure 4. Evolution of the distances from the regions fronts to the flaring PILs in all cases, with red (green) for B_h -increase region (flare ribbons). The subtitles indicate case numbers in Table 1. The vertical lines mark the flares start. The shaded regions mark the co-existence duration of B_h -increase and flare ribbons.

Török, T., & Kliem, B. 2005, *The Astrophysical Journal*, 630, L97, doi: [10.1086/462412](https://doi.org/10.1086/462412)

Wang, H., & Liu, C. 2015, *Research in Astronomy and Astrophysics*, 15, 145, doi: [10.1088/1674-4527/15/2/001](https://doi.org/10.1088/1674-4527/15/2/001)

Wang, H., Liu, C., Wang, S., et al. 2013, *ApJL*, 774, doi: [10.1088/2041-8205/774/2/L24](https://doi.org/10.1088/2041-8205/774/2/L24)

Wang, H., Spirock, T. J., Qiu, J., et al. 2002, *ApJ*, 576, 497, doi: [10.1086/341735](https://doi.org/10.1086/341735)

Wang, J., Shi, Z., Wang, H., & Lue, Y. 1996, *ApJ*, 456, 861, doi: [10.1086/176703](https://doi.org/10.1086/176703)

Wang, J., Simões, P. J. A., & Fletcher, L. 2018, *ApJ*, 859, 25, doi: [10.3847/1538-4357/aabc0e](https://doi.org/10.3847/1538-4357/aabc0e)

Wang, S., Liu, C., Deng, N., & Wang, H. 2014, *ApJ*, 782, L31, doi: [10.1088/2041-8205/782/2/L31](https://doi.org/10.1088/2041-8205/782/2/L31)

Wang, S., Liu, C., Liu, R., et al. 2012, *ApJ*, 745, L17, doi: [10.1088/2041-8205/745/2/L17](https://doi.org/10.1088/2041-8205/745/2/L17)

Wang, W., & Liu, R. 2021, *A&A*, 647, 1, doi: [10.1051/0004-6361/202039732](https://doi.org/10.1051/0004-6361/202039732)

Wheatland, M. S., Melrose, D. B., & Mastrano, A. 2018, *ApJ*, 864, 159, doi: [10.3847/1538-4357/aad8ae](https://doi.org/10.3847/1538-4357/aad8ae)

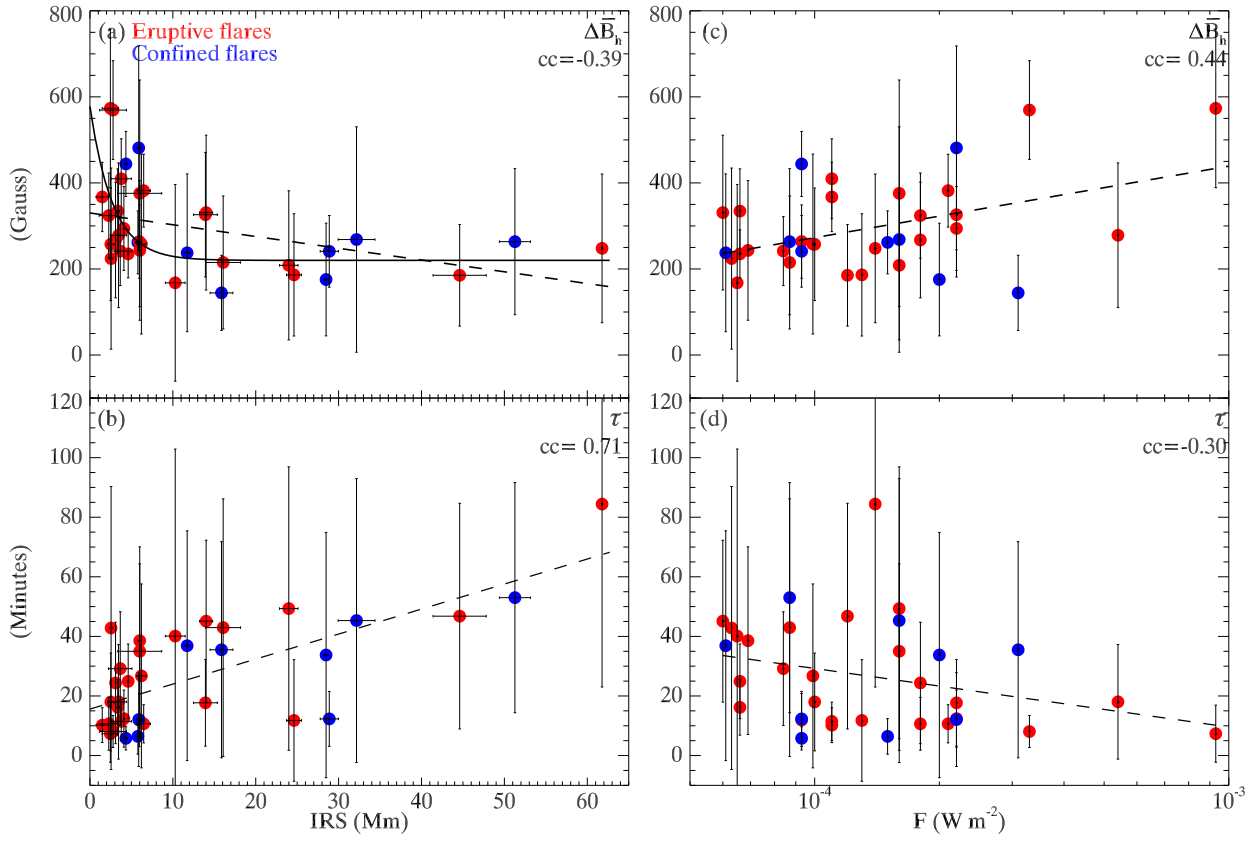


Figure 5. (a)-(b) Scatter plots between two B_h -increase parameters and initial ribbons separation (IRS). The solid curve in (a) represents an exponential fitting. The dashed line represents the linear fitting. “cc” indicates the correlation coefficient. (c)-(d) Scatter plots between the parameters and flare magnitude shown for comparison.